Hindawi
Advances in Condensed Matter Physics
Volume 2019, Article ID 8148392, 12 pages
https://doi.org/10.1155/2019/8148392

*Research Article*

# Prediction of the Linear and Nonlinear Optical Properties of a Schiff Base Derivatives via DFT

**Clodoaldo Valverde**,[1,2] **Ítalo Nuta Ribeiro**,[1] **João Victor B. Soares**,[1] **Basílio Baseia**,[3,4] **and Francisco A. P. Osório**[4,5]

[1]*Laboratório de Modelagem Molecular Aplicada e Simulação (LaMMAS), Campus de Ciências Exatas e Tecnológicas, Universidade Estadual de Goiás, 75001-970 Anápolis, GO, Brazil*
[2]*Universidade Paulista, 74845-090 Goiânia, GO, Brazil*
[3]*Departamento de Física, Universidade Federal da Paraíba, 58.051-970 João Pessoa, PB, Brazil*
[4]*Instituto de Física, Universidade Federal de Goiás, 74.690-900 Goiânia, GO, Brazil*
[5]*Escola de Ciências Exatas e da Computação, Pontifícia Universidade Católica de Goiás, 74605-220 Goiânia, GO, Brazil*

Correspondence should be addressed to Clodoaldo Valverde; valverde@ueg.br

Received 9 December 2018; Revised 20 February 2019; Accepted 21 February 2019; Published 1 April 2019

Academic Editor: Charles Rosenblatt

Copyright © 2019 Clodoaldo Valverde et al. This is an open access article distributed under the Creative Commons Attribution License, which permits unrestricted use, distribution, and reproduction in any medium, provided the original work is properly cited.

In this work, the density functional theory (DFT) calculation combined with a polarizable continuum model (PCM) was used to study the solvent media effects on the electrical and geometrical behaviors of the Schiff-base derivative, (E)-4-[({4-[(pyridin-2-ilmetilideno)amino]phenyl}amino)-metil]fenol (EPAF). The linear and nonlinear optics parameters, as the dipole moment, linear polarizability, and first and second hyperpolarizabilities, were calculated at DFT/B3LYP/6-311+G(d) level, for the EPAF molecule in several solvent media. The dynamic behavior of the Hyper-Rayleigh Scattering (HRS) first hyperpolarizability was studied as function of the electric field frequency. The results presented for HRS first hyperpolarizability suggest that the studied crystal has good nonlinear optical properties. In addition, the gap energy was calculated from the HOMO-LUMO energies difference in several solvent media. The EPAF crystal intermolecular interactions were studied by the Hirshfeld surface analysis. The third-order electric susceptibility $\chi^{(3)}$ of the crystal EPAF was also calculated, indicating the EPAF crystal as a promising candidate for NLO applications in photonic and optoelectronic devices.

## 1. Introduction

In recent years, the use of organic crystals as nonlinear optical (NLO) materials has been growing motivated by the easy manipulation of these crystals, which allow controlling the material NLO properties [1]. Studies of nonlinear optical processes contribute significantly to the development of photonics [2, 3], spectroscopy [4, 5], fiber optic lines [4], optical switches [6], frequency converters [7], electrooptic modulators [8], and data transmission network, among others [9] and still in numerous applications in the medical and pharmacological sectors [10–12]. The compounds that have a high nonlinearity are of great interest for the field of nonlinear optics, since they make up the manufacture of devices that operate with high speed [9, 13].

Schiff bases are aldehyde or ketone-like compounds in which the carbonyl group is replaced by animine or azomethine group. They are widely used for industrial purposes and also exhibit a broad range of biological activities, as antibacterial, anticancer, anti-inflammatory, and antitoxic properties as stated by Lozier et al. [14]. The compounds of this group have a potential for use in optical memory device, because they form coordinating or grid polymers. Recently, a Schiff base derivative (E)-4-[({4-[(pyridin-2-ilmetilideno)amino]phenyl}amino)-metil]fenol (EPAF) with molecular formula $C_{19}H_{17}N_3O$ has been synthesized, crystallized, and structurally characterized by Faizi et al. [15]. Also, these authors used the density functional theory (DFT) at B3LYP/6-311G(d,p) level to calculate geometrical parameters of the EPAF single molecule and compare them with the

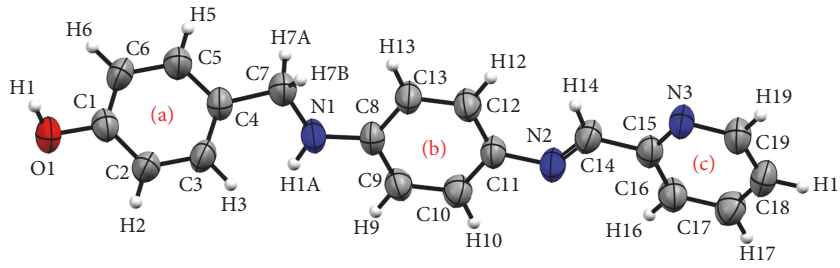


Figure 1: A view of the EPAF molecule showing the atom labeling scheme.

obtained X-ray results and verified a good agreement with the experimental data.

In this work, we study the effect of several solvent media on geometry and the electrical parameters of the EPAF molecule. The EPAF geometry optimization was performed in the gas phase and in various solvent media using DFT at level CAM-B3LYP/6-311+G(d). The overlap between the X-ray data for EPAF molecules with the DFT results in several solvent media has shown a big variation of the torsion angles between the rings. The solvent media effects on EPAF molecule static electrical parameters as dipole moment, linear polarizability, first hyperpolarizability, and the second hyperpolarizability are studied. The behaviors of the EPAF Hyper-Rayleigh Scattering (HRS) first hyperpolarizability in several solvent media as function of the electric field frequencies and of the static dielectric constant value were analyzed. Also the energies of the highest occupied molecular orbital (HOMO) and lowest unoccupied molecular orbital (LUMO), as the gap energies in several solvent media, have been calculated. Also a Hirshfeld surface analysis is presented to complement the EPAF crystal study of [15].

## 2. Methodology

The EPAF compound was crystallized in a monoclinic space group $P2_1/c$ [15] (see Figure 1) with the following crystallographic data: a = 10.55652 (7), b = 7.9136 (6), c = 20.8153 (13), $\alpha = 90^\circ$, $\gamma = 90^\circ$, and $\beta = 118.408^\circ$, unit cell volume 1530.77 Å, with four molecules in the unit cell (Z = 4). The EPAF molecule is nonplanar, with the phenolic ((a)) and pyridine rings ((c)) being inclined to the central benzene ring ((b)).

*2.1. Hirshfeld Surface.* Hirshfeld surface (HS) analysis serves as a powerful tool for obtaining crucial information about the intermolecular interaction of molecular crystals. The size and shape of the Hirshfeld surface allow the visualization and investigation of both qualitative and quantitative intermolecular crystal bonds. Thus, the HS surface is obtained and two distances are defined, the distance from the point to the nearest atom off the surface ($d_e$) and the distance to the nearest atom within the surface ($d_i$). The identification of the regions of particular importance to intermolecular interactions is obtained by mapping normalized contact distance ($d_{norm}$), defined by

$$d_{norm} = \frac{d_i - r_i^{vdW}}{r_i^{vdW}} + \frac{d_e - r_e^{vdW}}{r_e^{vdW}}, \quad (1)$$

where $r_i^{vdW}$ and $r_e^{vdW}$ are the van der Waals radii of the atoms. Studies of the $\pi \ldots \pi$ interactions were performed analyzing the surface shape index, where this interaction type can be identified through the red and blue triangle, one facing the other [18].

*2.2. Computational Details.* The solvent media effects on the electric parameters of the EPAF molecule were studied employing the polarizable continuum model (PCM). First the geometry optimization calculations were performed in gas phase and after in nineteen solvent media, both method using the DFT at B3LYP/6-311+G(d) level.

In the present study, the total dipole moment, average linear polarizability $\langle\alpha\rangle$, and anisotropy of the linear polarizability $\Delta\alpha$ of the title compounds have been calculated using the following expression:

$$\mu = \left(\mu_x^2 + \mu_y^2 + \mu_z^2\right)^{1/2}, \quad (2)$$

$$\langle\alpha\rangle = \frac{\alpha_{xx} + \alpha_{yy} + \alpha_{zz}}{3}, \quad (3)$$

$$\Delta\alpha = 2^{-1/2}\left[\left(\alpha_{xx} - \alpha_{yy}\right)^2 + \left(\alpha_{yy} - \alpha_{zz}\right)^2 + \left(\alpha_{zz} - \alpha_{xx}\right)^2 + 6\left(\alpha_{xz}{}^2 + \alpha_{xy}{}^2 + \alpha_{yz}{}^2\right)\right]^{1/2}. \quad (4)$$

The total and HRS (Hyper Rayleigh Scattering) molecular first hyperpolarizabilities are given by

$$\beta_{total} = \left[\left(\beta_{xxx} + \beta_{xyy} + \beta_{xzz}\right)^2 + \left(\beta_{yyy} + \beta_{yxx} + \beta_{yzz}\right)^2 + \left(\beta_{zxx} + \beta_{zyy} + \beta_{zzz}\right)^2\right]^{1/2}, \quad (5)$$

and

$$\langle\beta_{HRS}\rangle = \sqrt{\langle\beta_{ZZZ}^2\rangle + \langle\beta_{XZZ}^2\rangle}, \quad (6)$$

where $X$-direction is assumed as the fundamental light beam propagation and polarized in the $Z$-direction and $\langle\beta_{ZZZ}^2\rangle$ and $\langle\beta_{XZZ}^2\rangle$ are macroscopic averages calculated from the first hyperpolarizability components ($\beta_{ijk}$)[19, 20] through the

Table 1: The HRS first hyperpolarizability $\delta_n$ coefficients.

| | |
|---|---|
| $\delta_1 = \sum_i \beta_{iii}^2$, | $\delta_7 = \sum_{i,j,k} \beta_{ijj}\beta_{ikk}$, |
| $\delta_2 = \sum_{i,j} \beta_{iii}\beta_{ijj}$, | $\delta_8 = \sum_{i,j,k} (\beta_{jij} + \beta_{jji})(\beta_{kik} + \beta_{kki})$, |
| $\delta_3 = \sum_{i,j} \beta_{iii}(\beta_{jij} + \beta_{jji})$, | $\delta_9 = \sum_{i,j,k} \beta_{ijj}(\beta_{kik} + \beta_{kki})$, |
| $\delta_4 = \sum_{i,j} \beta_{ijj}^2$, | $\delta_{10} = \sum_{i,j,k} (\beta_{ijk} + \beta_{ikj})^2$, |
| $\delta_5 = \sum_{i,j} \beta_{ijj}(\beta_{jij} + \beta_{jji})$, | $\delta_{11} = \sum_{i,j,k} (\beta_{ijk} + \beta_{ikj})(\beta_{jjk} + \beta_{jki})$. |
| $\delta_6 = \sum_{i,j} (\beta_{jij} + \beta_{jji})^2$ | |

expressions. Hyper-Rayleigh Scattering (HRS) components ($\beta_{ijk}$) [19, 20] were calculated through the expressions

$$\begin{aligned}\left\langle \beta_{ZZZ}^2 \right\rangle &= \frac{1}{210}\left(30\delta_1 + 12\left(\delta_2 + \delta_3 + \delta_5\right) + 6\left(\delta_4 + \delta_6\right)\right. \\ &\quad \left. + 2\left(\delta_7 + \delta_8 + \delta_{11}\right) + 4\delta_9 + \delta_{10}\right), \\ \left\langle \beta_{XZZ}^2 \right\rangle &= \frac{1}{210}\left(6\left(\delta_1 - \delta_3 - \delta_5 + \delta_7\right) + 8\delta_2 + 18\delta_4\right. \\ &\quad \left. + 4\delta_6 - \delta_8 - 2\delta_9 + 3\delta_{10} - \delta_{11}\right),\end{aligned} \tag{7}$$

in which the coefficients $\delta_n$ are defined in Table 1. In this case, we adopted the laboratory system of reference by the *X*, *Y*, and *Z* coordinates, and the molecular system of reference by the *x*, *y*, and *z* coordinates.

The average second molecular hyperpolarizability is given by

$$\langle \gamma \rangle = \frac{1}{15} \sum_{i,j=x,y,z} \left(\gamma_{iijj} + \gamma_{ijij} + \gamma_{ijji}\right). \tag{8}$$

Using the Kleymann symmetry, the $\langle\gamma\rangle$-value can be calculated through the following expression:

$$\begin{aligned}\langle \gamma \rangle &= \frac{1}{5}\left[\gamma_{xxxx} + \gamma_{yyyy} + \gamma_{zzzz}\right. \\ &\quad \left. + 2\left(\gamma_{xxyy} + \gamma_{xxzz} + \gamma_{yyzz}\right)\right].\end{aligned} \tag{9}$$

All computational calculations related to the linear and nonlinear electric parameters of the compounds were performed in the *GAUSSIAN* 09 program [21].

*2.3. Frontiers Molecular Orbital.* In order to verify the EPAF molecule stability in the several solvent media, the highest occupied orbital energy (HOMO), which has an electron-donor character, and the lowest unoccupied molecular orbital energy (LUMO), which has an electron-acceptor character, were calculated. The molecule ability to donate or receive electrons is greater as the HOMO-value or the LUMO-value, respectively [22]. The energy difference between HOMO and LUMO gives the GAP energy, a parameter which is directly related to the stability of the compound [23].

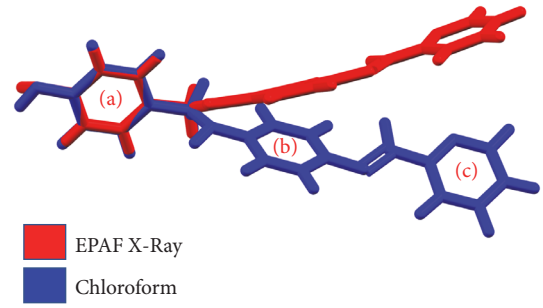


Figure 2: Overlap between the molecular structure determined by X-ray (in red) and in Chloroform (in blue). The ring (a) was used as anchorage.

*2.4. Solvent Media.* The solvent medium polarity is related to it solvability. Defining the polarity concept quantitatively is very difficult, and controversial; in this work, we will use the concept of polarity defined by the scale $E_T^N$ (normalized transition energy) of Dimroth and Reichardt [16]. The $E_T^N$-value is based on the transition energy for the longest-wavelength solvatochromic absorption band of the pyridinium N-phenolate betaine dye (see Table 2). Here, solvent media with static dielectric constant ($\varepsilon$) value smaller than 5 will be considered as nonpolar.

All computational calculations related to the linear and nonlinear electric parameters of the compounds were performed in the *GAUSSIAN* 09 program [21].

## 3. Results and Discussions

*3.1. Structural Commentary.* The optimized geometry in gas phase and in several solvent media of the EPAF structure was analyzed through the root mean square deviation (RMSD) of the overlap between the molecular geometry determined by X-ray and the theoretical results obtained in the presence of solvent media; the H-atoms were disregarded in view of their uncertainties in X-ray position refinement. All the optimized geometries of the EPAF molecule calculated in various solvent media are in the Supplementary Materials (see Tables S1 – S20). The optimized geometry results in chloroform using the ring (a) as anchorage are presented in Figure 2; the RMSD is 0.5460 a.u. Table 3 shows the RMSD for the optimized geometry in several solvent media; as can be observed, the RMSD-values for nonpolar solvent media (argon, heptane, and toluene) are approximately 0.50 a.u. and for the others it is 0.54 a.u.

The solvent media presence causes a significant deviation of the RMSD parameter between the X-ray geometry data and the theoretical results, as can be seen in Figure 2 for the chloroform (RMSD=0.544). The $C4 - C7 - N1 - C8$ and $C11 - N2 - C14 - C15$ torsion angles change due to the solvent medium effects (chloroform) from -166.3° (X-ray data) to +176.24 and +176.4 (X-ray data) to -177.72°, respectively. This effect occurs due to the negative charge transfer to the hydroxyl bond to the terminal phenolic ring (C1–C6). Table S21 (Supplementary Materials) shows the

Table 2: Solvent media polarity parameter and static dielectric constant, as in ref. [16].

| Solvent medium | $E_T^N$ | $\varepsilon$ | |
|---|---|---|---|
| Water | 1.00 | 78.355 | protic |
| Formamide | 0.775 | 108.940 | protic |
| Methanol | 0.762 | 32.613 | protic |
| FormicAcid | 0.728 | 51.100 | protic |
| n-MethylFormamide-mixture | 0.722 | 181.560 | protic |
| Ethanol | 0.654 | 24.852 | protic |
| 1-Butanol | 0.586 | 17.332 | protic |
| Acetonitrile | 0.460 | 35.688 | aprotic |
| DMSO | 0.444 | 46.826 | aprotic |
| 2-Methyl-2-Propanol | 0.389 | 12.470 | protic |
| Acetone | 0.355 | 20.493 | aprotic |
| DiChloroEthane | 0.327 | 10.125 | aprotic |
| DichloroMethane | 0.309 | 8.930 | aprotic |
| Chloroform | 0.259 | 4.711 | nonpolar |
| Tetrahydrofuran | 0.207 | 7.426 | aprotic |
| ChloroBezene | 0.188 | 5.697 | aprotic |
| Toluene | 0.099 | 2.374 | nonpolar |
| Heptane | 0.012 | 1.911 | nonpolar |

Table 3: Comparison of selected geometric data for EPAF (°) from calculated DFT-Solvent and X-ray data.

| | $\varepsilon$ | RMSD | C6-C1-O1 | C8-N1-C7 | N1-C7-C4 | C14-N2-C11 | N2-C14-C15 | N3-C15-C14 |
|---|---|---|---|---|---|---|---|---|
| EPAF-X-Ray | | | 120.3 | 123.4 | 112.3 | 121.5 | 122.2 | 115.9 |
| Gas-phase | 1.000 | 0.498 | 122.9 | 122.7 | 110.8 | 121.5 | 122.1 | 115.4 |
| Argon | 1.430 | 0.502 | 122.8 | 122.7 | 110.8 | 121.6 | 122.1 | 115.4 |
| Heptane | 1.911 | 0.502 | 122.8 | 122.8 | 110.8 | 121.6 | 122.2 | 115.4 |
| Toluene | 2.374 | 0.501 | 122.8 | 122.8 | 110.8 | 121.6 | 122.2 | 115.4 |
| Chloroform | 4.711 | 0.546 | 122.8 | 122.7 | 110.8 | 121.6 | 122.3 | 115.3 |
| ChloroBezene | 5.697 | 0.542 | 122.8 | 122.7 | 110.8 | 121.6 | 122.3 | 115.3 |
| Tetrahydrofuran | 7.426 | 0.544 | 122.8 | 122.7 | 110.7 | 121.6 | 122.4 | 115.3 |
| DichloroMethane | 8.930 | 0.544 | 122.7 | 122.8 | 110.7 | 121.6 | 122.4 | 115.3 |
| DiChloroEthane | 10.125 | 0.544 | 122.7 | 122.8 | 110.7 | 121.6 | 122.4 | 115.3 |
| 2-Methyl-2-Propanol | 12.470 | 0.543 | 122.7 | 122.7 | 110.7 | 121.6 | 122.4 | 115.3 |
| 1-Butanol | 17.332 | 0.543 | 122.7 | 122.7 | 110.7 | 121.6 | 122.4 | 115.3 |
| Acetone | 20.493 | 0.543 | 122.7 | 122.7 | 110.7 | 121.6 | 122.4 | 115.3 |
| Ethanol | 24.852 | 0.543 | 122.7 | 122.7 | 110.7 | 121.6 | 122.4 | 115.3 |
| Methanol | 32.613 | 0.543 | 122.7 | 122.7 | 110.7 | 121.6 | 122.4 | 115.3 |
| Acetonitrile | 35.688 | 0.543 | 122.7 | 122.7 | 110.7 | 121.7 | 122.4 | 115.3 |
| DMSO | 46.826 | 0.543 | 122.7 | 122.7 | 110.7 | 121.7 | 122.4 | 115.2 |
| FormicAcid | 51.100 | 0.543 | 122.7 | 122.7 | 110.7 | 121.7 | 122.4 | 115.2 |
| Water | 78.355 | 0.543 | 122.7 | 122.7 | 110.7 | 121.7 | 122.4 | 115.2 |
| Formamide | 108.940 | 0.543 | 122.7 | 122.7 | 110.7 | 121.7 | 122.4 | 115.2 |
| n-MethylFormamide-mixture | 181.560 | 0.542 | 122.7 | 122.7 | 110.7 | 121.7 | 122.4 | 115.2 |

charges of the atoms of the molecule under the effect of several solvent media using the PCM method calculated via DFT (CAM-B3LYP/6-311+G(d)) using the electrostatic model ChelpG. The ChelpG fit of the pyridine ring and hydroxyl charges are 0.04$e$ and −0.238$e$ both in chloroform medium (see the ChelpG charges for all atoms in Table S21 of the Supplementary Materials).

DFT results for the EPAF optimized geometry in gas phase and in several solvent media are shown in Table 3. The C7—N1—C8 angle presents a reduction of 0.59% for both polar and nonpolar solvent. In the solvent media, the C6—C1—O1 angle increased around 2.0% and the N1—C7—C4 angle remains invariable in gas phase, toluene, heptane, and argon. This angle has increased 0.08% and

Table 4: DFT static results for the EPAF electrical parameters.

| $\varepsilon$ | $\langle\gamma(0;0,0,0)\rangle$ $10^{-36}$esu | $\beta_{\|z}(0;0,0)$ $10^{-30}$esu | $\langle\alpha(0;0)\rangle$ $10^{-24}$esu | $\mu$ (D) |
|---|---|---|---|---|
| 1.000 | 170 | -0.230 | 42 | 2.86 |
| 1.430 | 220 | -0.200 | 44 | 3.01 |
| 1.911 | 254 | -0.157 | 46.4 | 3.12 |
| 2.374 | 280 | -0.127 | 47.7 | 3.19 |
| 4.711 | 351 | -0.611 | 51 | 3.44 |
| 5.697 | 367 | -0.581 | 51.7 | 3.48 |
| 7.426 | 387 | -0.602 | 52.6 | 3.53 |
| 8.930 | 399 | -0.602 | 53.1 | 3.57 |
| 10.125 | 406 | -0.603 | 53.4 | 3.59 |
| 12.470 | 416 | -0.595 | 53.9 | 3.61 |
| 17.332 | 435 | -0.605 | 54.7 | 3.67 |
| 20.493 | 440 | -0.607 | 54.9 | 3.68 |
| 24.852 | 446 | -0.609 | 55.2 | 3.70 |
| 32.613 | 448 | -0.609 | 55.3 | 3.70 |
| 35.688 | 452 | -0.609 | 55.5 | 3.72 |
| 46.826 | 454 | -0.608 | 55.6 | 3.72 |
| 51.100 | 458 | -0.612 | 55.6 | 3.73 |
| 78.355 | 461 | -0.604 | 55.9 | 3.74 |
| 108.940 | 464 | -0.604 | 56.0 | 3.75 |

0.16% and in chloroform and in the polar solvent medium, respectively. Also the C14—N2—C11 angle increased 0.08% and 0.16% for solvent media with $\varepsilon < 37$ and $\varepsilon > 37$, respectively. The X-ray and theoretical results in the solvent media for the angles, N2—C14—C15 and N3—C15—C14, are practically the same.

*3.2. HOMO-LUMO.* In this section, the HOMO and LUMO results for the EPAF molecule in several solvent media are presented. The HOMO and LUMO orbital and the gap energy values in the solvent medium n-methyl formamide mixture and in gas phase are shown in Figure 3. All HOMO-LUMO figures are in the Supplementary Materials (see Figures S1 – S18).

As can be seen in Figure 4, the gap energy decreases with the increasing of the dielectric constant value of the solvent medium. The gap energy ($E_G$) goes from 3.466 eV ($\varepsilon$=1.0) to 3.349 eV ($\varepsilon$=182.4) indicating that the maximum absorption wavelengths ($\lambda_{max}=hc/E_G$) fall into the ultra violet (UV) region. The gap energy is an important parameter that determines the chemical properties of a molecule as the kinetic stability, chemical reactivity, optical polarizability, etc. Larger values of the gap energy are directly related to greater stability of the molecule.

All values of HOMO-LUMO and gap energy of the EPAF molecule calculated in various solvent media are in the Supplementary Materials (see Tables S22).

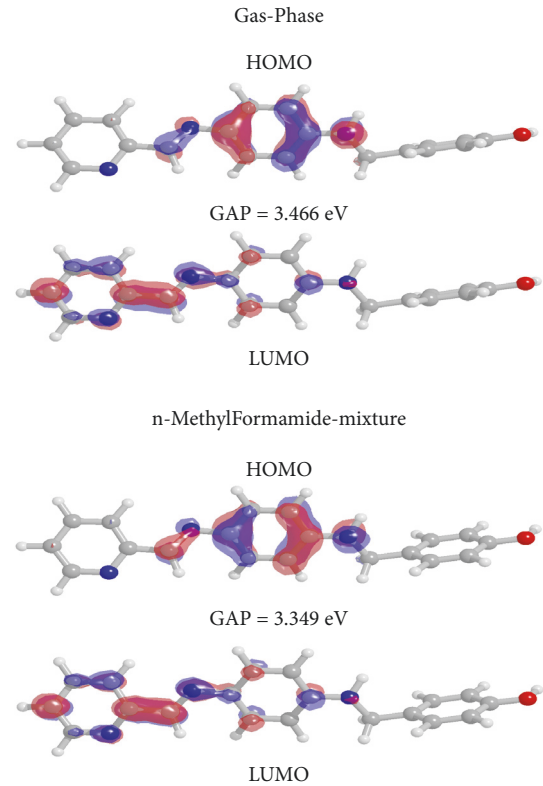


Figure 3: HOMO and LUMO in n- methyl formamide mixture.

*3.3. Nonlinear Optical Properties in Solvent Medium.* Table 4 shows the DFT/B3LYP/6-311+G(d) static results for the total dipole moment ($\mu_{tot}$), the isotropic linear polarizability $\langle\alpha(0;0)\rangle$, the first hyperpolarizability parallel to the dipole moment ($\beta_{||}z(0;0,0)$), and the second hyperpolarizability $\langle\gamma(0;0,0,0)\rangle$ both in gas-phase and in several solvent media. As can be noted, the values of $\mu$, $\langle\alpha(0;0)\rangle$ and $\langle\gamma(0;0,0,0)\rangle$ increase with the increasing of the $\varepsilon$-values (Figures 5(a), 5(b),

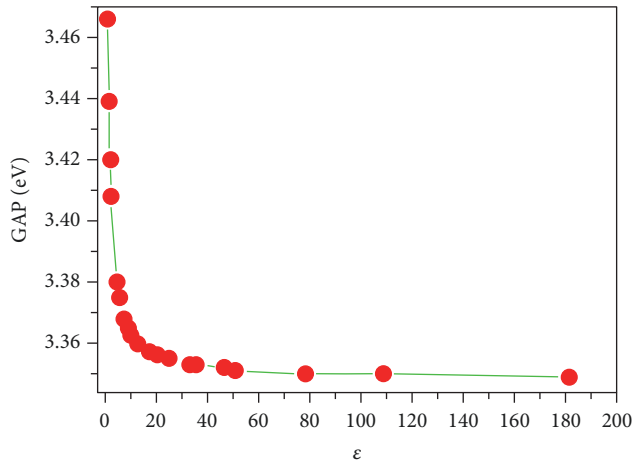


Figure 4: Gap energy as function of the dielectric constant values.

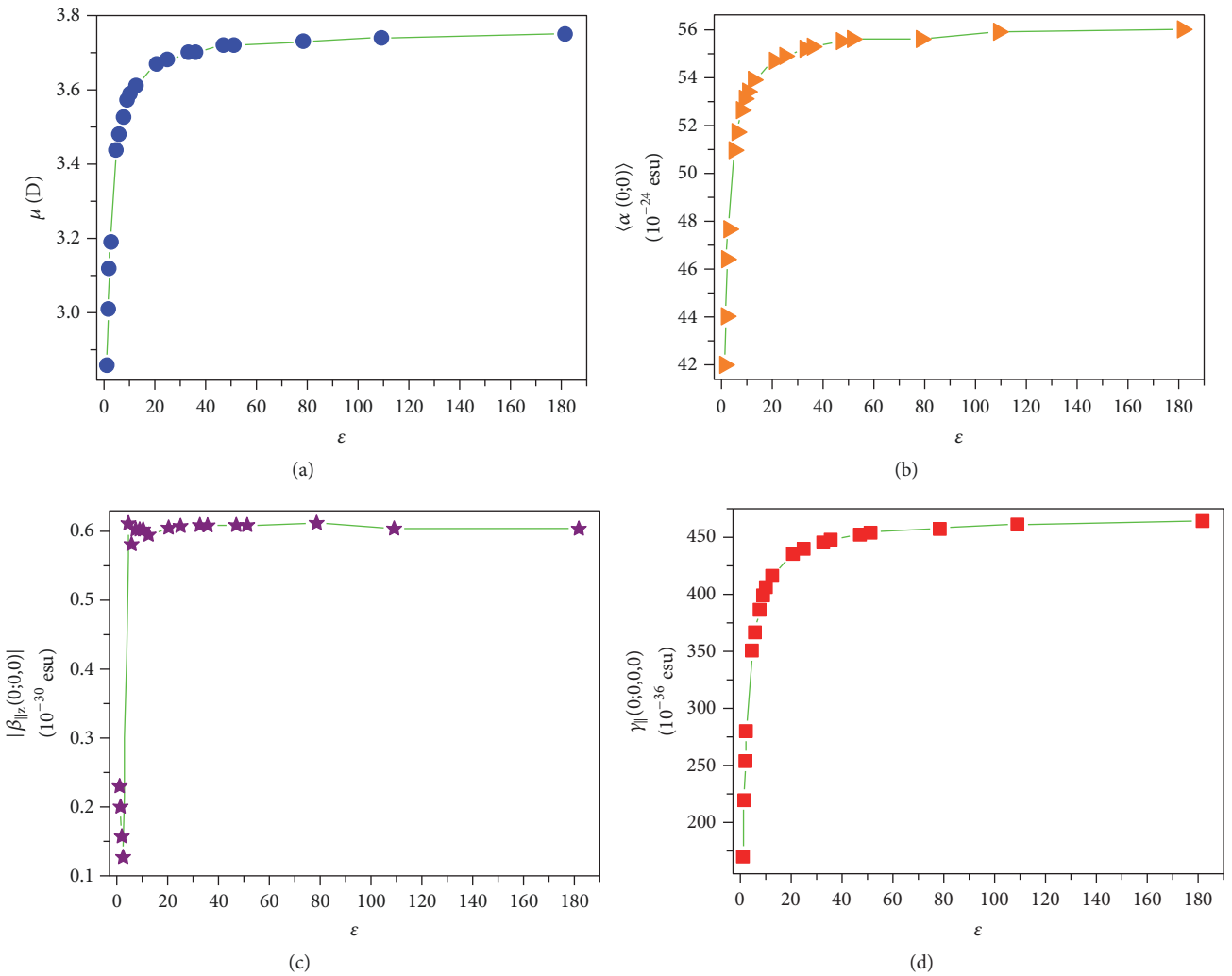


Figure 5: DFT static results for the EPAF electric parameter as function of the $\varepsilon$-value.

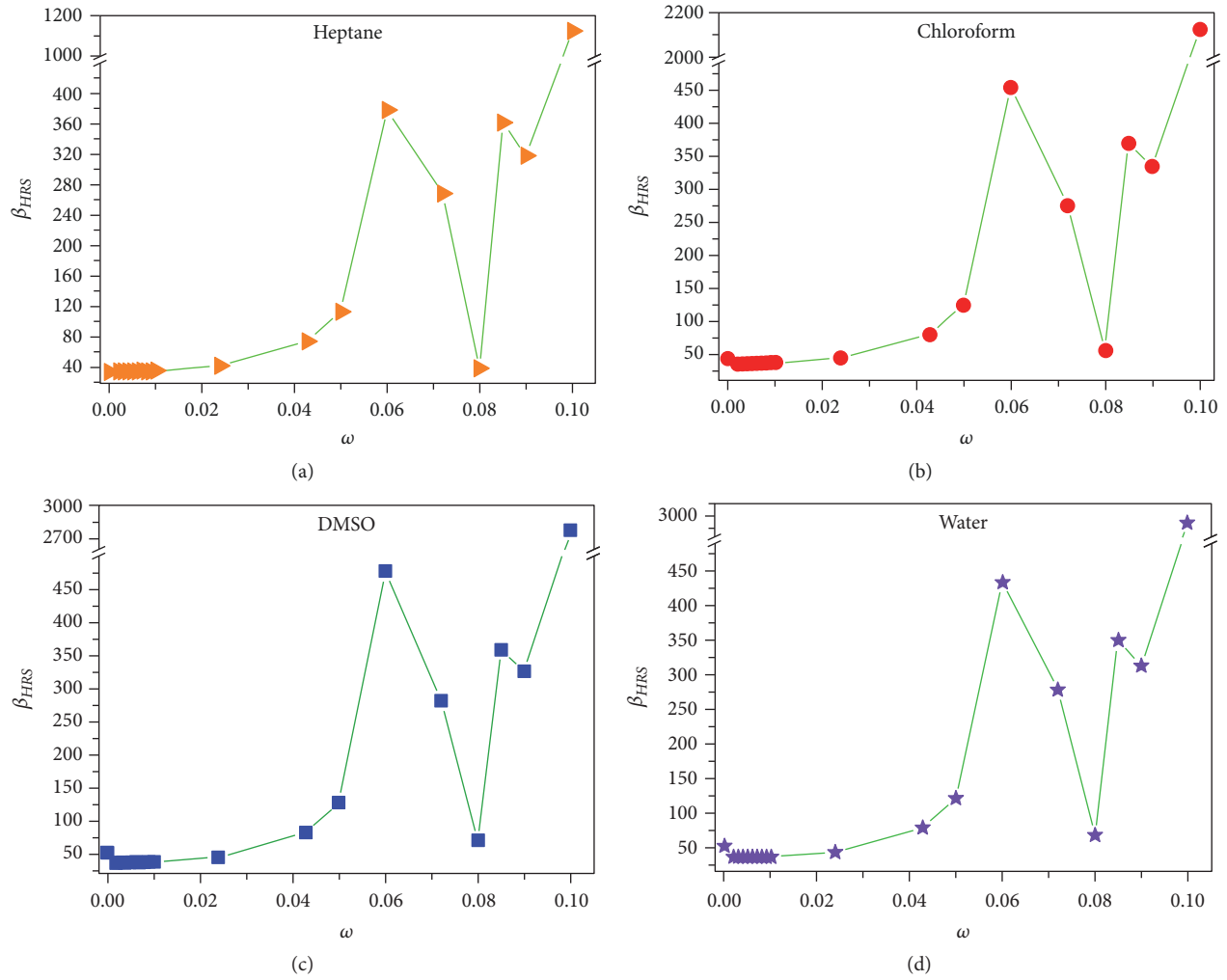


FIGURE 6: Dynamic HR Scattering first hyperpolarizability as function of the field frequency ($\omega$) in a.u..

and 5(d)). In all solvent media, the $\beta_{||}z(0;0,0)$-values are negative, and for $\varepsilon \geq 5$ they oscillate around $0.6 \times 10^{-30} esu$; however, the $|\beta_{||}z(0;0,0)|$ increases with the increasing of the $\varepsilon$-values, as can be seen in Figure 5(c).

From Table 4, it can be verified that the first and second hyperpolarizabilities present the greater variation due to the solvent medium presence, from heptane ($\varepsilon$=1.911) to n-methyl formamide mixture ($\varepsilon$=181.56); the values of $|\beta_{||}z(0;0,0)|$ and $\langle\gamma(0;0,0,0)\rangle$ present a percentage increasing of 285% and 83% (see Figures 5(c) and 5(d) ). However, the character, protic or aprotic, seems to not influence the results, but the nonpolar solvent media present a smaller value of the total dipole moment, and this can be understood taking into account that the polar solvent media the OH present greater increasing of the negative charge, and similar effect can be verified for other electric parameters (Figure 5).

The DFT static results for the $\beta_{HRS}$-values obtained from (6) in a solvent medium are several orders of magnitude higher than the values of $\beta_{||z}(0;0,0)$. While as shown in Table 3 for the solvent media the absolute values of $\beta_{||z}(0;0,0)$ go from 0.2 to 0.6 (in units of $10^{-30} esu$), $\beta_{HRS}(0,0,0)$ go from 24.4 to 53.0 (in units of $10^{-30} esu$). Table S23 of the Supplementary Material shows the static and dynamic $\beta_{HRS}$-values for the gas phase and all the solvent media. The behaviors of the static and dynamic HRS first hyperpolarizability in the solvent media are similar; therefore, in Figure 6, the results for $\beta_{HRS}$ as function of the field frequency ($\omega$) are shown for only four solvents, namely, heptane ($\varepsilon$=1.911, nonpolar), chloroform ($\varepsilon$=4.71; larger RMSD parameter), DMSO ($\varepsilon$=46.8; aprotic), and water ( $\varepsilon$=78.4; $E_T^N$=1). From Figure 6 and from Table S23, two resonant regions can be identified in the region $0.06 a.u. < \omega < 0.09 a.u.$ So we will work away from the transition region, because in this region it would be complicated for the experiment to work due to deleterious effects. We will study $\beta_{HRS}$ on the frequency of $\omega$=0.0428 a.u.(1064 nm).

We can also highlight that the protic or aprotic character and also the polarity of the solvent did not alter the HRS first hyperpolarizability behavior as a function of the frequency. The $\beta_{HRS}$-values increase with the increasing of the dielectric constant value (or with the decreasing of the gap energy) as can be seen in Figure 7. This effect can be explained by the increase of the hydroxyl group charge, which acts as an electrons receptor of the benzene ring, decreasing the

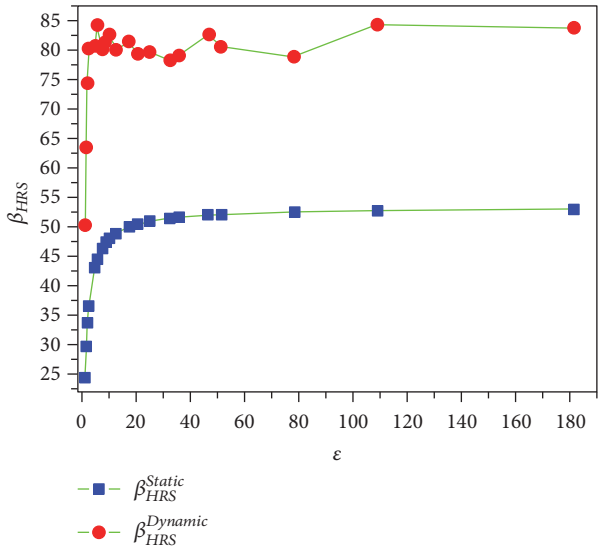


FIGURE 7: Static and dynamic (1064nm) HRS first hyperpolarizability as function of the $\varepsilon$-value.

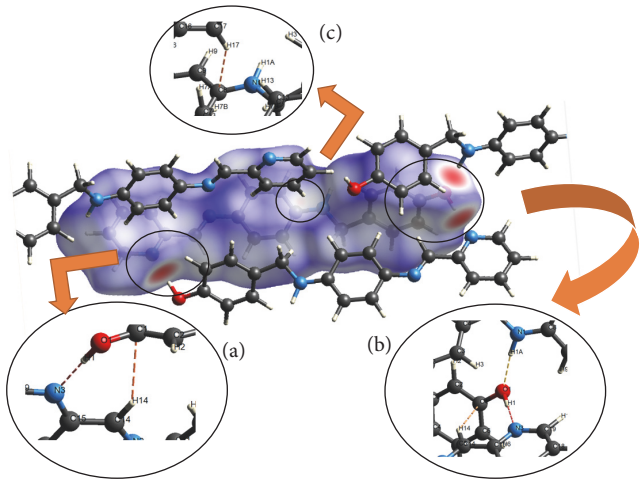


FIGURE 8: View of EPAF $d_{norm}$ surface showing the interactions O1-H1...N3 e C14-H14...C1 (a), N1-H1A...O, O1-H1...N3, and C14-H14...C1 (b), and C17-H17...C8 (c).

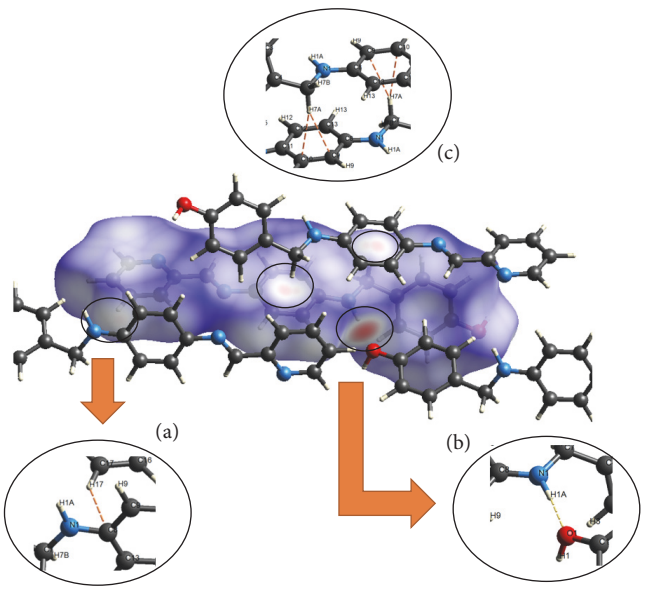


FIGURE 9: View of EPAF $d_{norm}$ surface showing the interactions (a) O1-H1...N3 and C14-H14...C1, (b) N1-H1A...O, O1-H1...N3, and C14-H14...C1, and (c) C17-H17...C8.

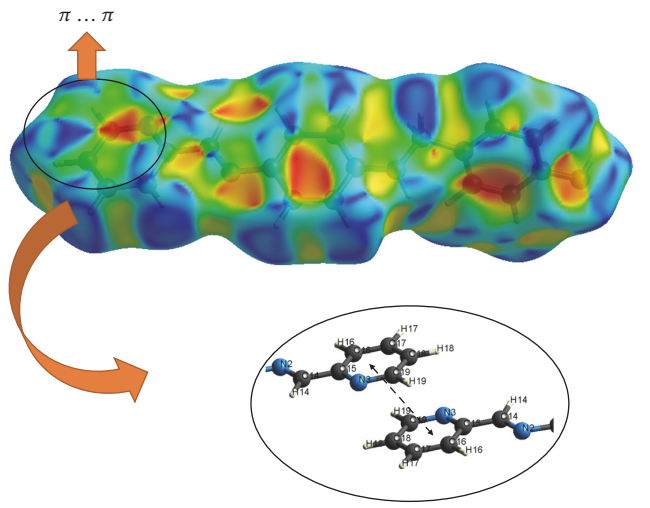


FIGURE 10: View of the shape index surface for EPAF showing the highlighted $\pi$...$\pi$ interaction.

electron density and the resonant stability, making it difficult to the electrophilic attack. In this case, the OH group acts as a disabling or metamanager. The values of $\beta_{HRS}$ in chloroform are 3 to 5 times higher than the 2,4,6-tris(benzylamino)-1,3,5-triazine [24] derivatives also measured in chloroform.

*3.4. Hirshfeld Surface Analyses.* The molecular structure of (E)-4-[({4-[(piridin-2-ilmetilideno) amino]fenil}amino)-metil]fenol (EPAF), $C_{19}H_{17}N_3O$, shows H bonds of the type $\pi$- $\pi$, C-H... $\pi$, C-H..C, O-H...N e N-H...O which contribute to the structure stability. Figure 8 shows the normalized Hirshfeld surface. Figure 8(a) shows the interactions O1-H1...N3 (D...A = 2.796 Å, D-H...A = 178.75°) and C14-H14...C1 (D...A = 3.640 Å, D-H...A = 146.17°). Figure 8(b) identifies the interactions N1-H1A...O1 (D...A = 2.982 Å, D-H...A = 170.07°), O1-H1...N3 (D...A = 2.796 Å, D-H...A = 178.75°), and C14-H14...C1 (D...A = 3.640 Å, D-H...A = 146.17°). Figure 8(c) shows the interactions C17-H17...C8 (D...A = 3,655 Å, D-H...A = 144.90°).

Figure 9(a) shows the interaction C17-H17...C8 (D...A = 3.655 Å, D-H...A = 144.90°), the same shown in Figure 9(c). The interaction N1-H1A...O1 (D...A = 2.982 Å, D-H...A = 170.07°) is shown in Figure 9(b) and the interactions C7-H7A...C9 (D...A = 3.723 Å, D-H...A = 151.80°) and C7-H7A...C10 (D...A = 3.681Å, D-H...A = 156.93°) are shown in Figure 9(c).

Figure 10 shows the shape index surface for the EPAF, where it is possible to see two triangles, one blue and the other

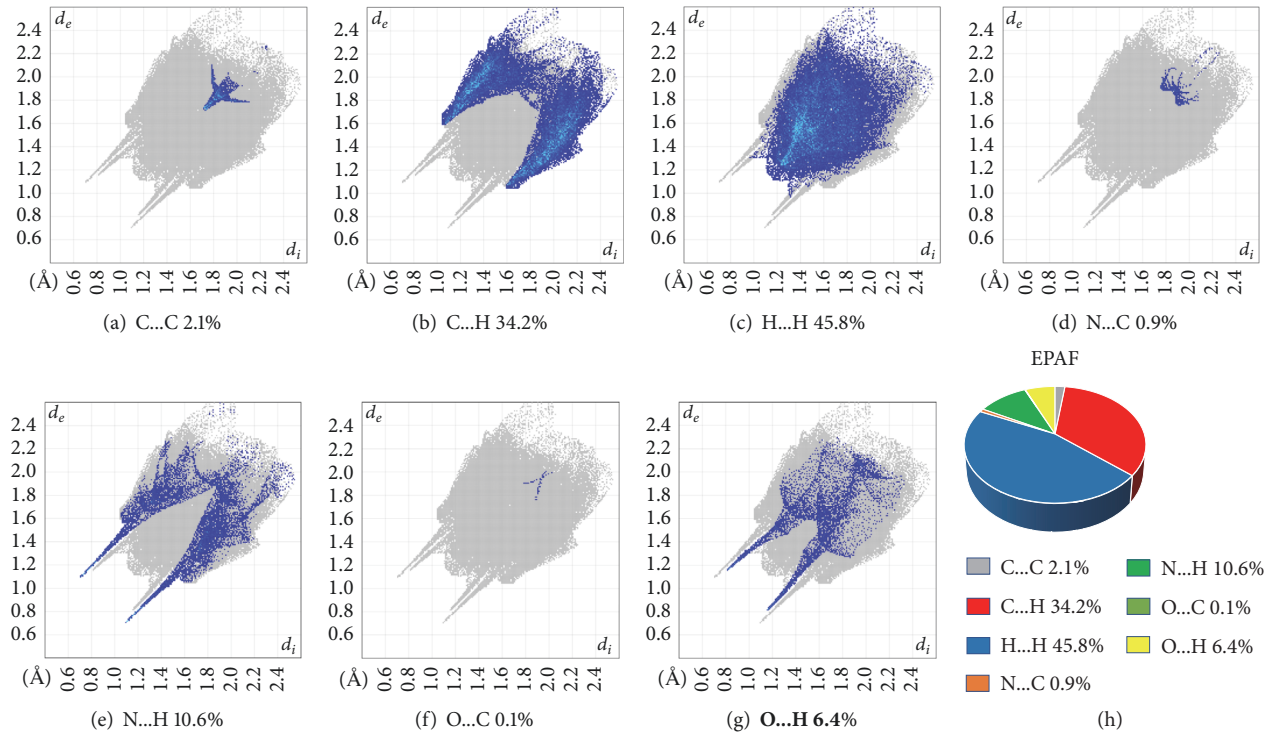


Figure 11: Fingerprint showing the 2D interactions of EPAF crystal.

red, one facing the other, representing the $\pi$- $\pi$ interaction ($\pi...\pi$ = 3,779 Å).

The fingerprints plots were used to analyze the amount of intermolecular interactions according to the nature and percentage of the interaction. Figures 11(a)–11(g) show the fingerprints for the EPAF; as we can see, the interaction with greater percentage in the whole crystal is the H..H with 45.8% of the interactions followed by the C. . .H with 34.2% of the interactions.

*3.5. Nonlinear Optical Properties of the EPAF Crystal.* The supermolecular (SM) method was used to simulate the EPAF crystal; details of the SM approach are given in the work of C. Valverde et al. [25]. To employ the SM approach, we have used the (x-ray) experimental geometry of the asymmetric unit of the EPAF. The packaging effects of the EPAF were modeled by constructing a bulk with the unit cells in a 9×9×9 configuration. Each unit cell contains four asymmetric units, totaling 2916 molecules in the monoclinic system, each atom surrounding the EPAF molecule (blue) being treated as a point charge (see scheme in Figure 12).

For the calculation, the average linear polarizability $\langle\alpha\rangle$ can be related to the linear refractive index ($n$) of the crystal via the Clausius-Mossotti relation, given by [26]:

$$\frac{n^2-1}{n^2+2} = \frac{4\pi N}{3}\langle\alpha\rangle, \tag{10}$$

where $N$ stands for the number of molecules per unit cell volume. The experimental quantity, the third-order electric

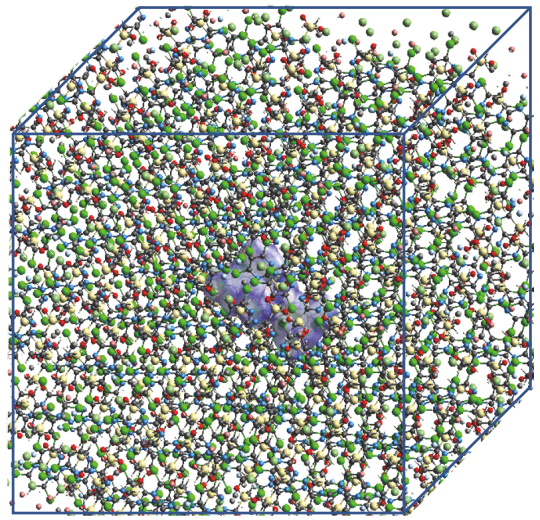

Figure 12: Scheme of the bulk representing the embedded molecule.

susceptibility $\chi^{(3)}$, is related to the second hyperpolarizability by

$$\chi^{(3)} = \frac{f^4 N\langle\gamma\rangle}{\epsilon_o V}, \tag{11}$$

where N is the number of molecules per unit cell volume (V) and $f$ is the Lorentz local field correction factor given by

$$f = \frac{\left(n^2+2\right)}{3}. \tag{12}$$

Table 5: The values of the linear polarizability (in $10^{-24}$ esu) were calculated CAM − B3LYP/6 − 311 + +$G(d, p)$ and for values of the second hyperpolarizability in (in $10^{-36}$ esu) we used CAM − B3LYP/6 − 311 + +$G(d, p)$ for EPAF embedded molecule ($\lambda = 532\ nm$).

| $\langle\alpha(-\omega, \omega)\rangle$ | $\langle\gamma(0; 0, 0, 0)\rangle$ | $\langle\gamma(-\omega; \omega, 0, 0)\rangle$ | $\langle\gamma(-\omega; \omega, \omega, -\omega)\rangle$ |
|---|---|---|---|
| 46.50 | 174.00 | 628.195 | 1082.39 |

Table 6: DFT/CAM-B3LYP/ 6-311++$G(d, p)$ results for the linear refractive index and third-order nonlinear susceptibility ($10^{-22}\ m^2/V^2$) for the case dynamic ($\lambda = 532\ nm$) of the EPAF crystal.

| Sample | $n(\omega)$ | $\chi^{(3)}(-\omega; \omega, \omega, -\omega)$ |
|---|---|---|
| EPAF (this work) | 2.02 | 6793.08 |
| (2E)-3-(3-methylphenyl)-1-(4-nitrophenyl)prop-2-en-1-one (3MPNP) [17] | 1.418 | 277.1 |
| (2E)-1-(4-bromophenyl)-3-[4-methylsulfanyl) phenyl]prop-2-en-1-one (4Br4MSP) [17] | 1.363 | 2.30 |
| (2E)-1-(3-bromophenyl)-3-[4(methylsulfanyl) phenyl]prop-2-en-1-one (3Br4MSP) [17] | 1.365 | 1.99 |
| (2E)-3[4(methylsulfanyl)phenyl]-1-(4-nitrophenyl)prop-2-en-1-one (4N4MSP) [17] | 1.360 | 2.37 |

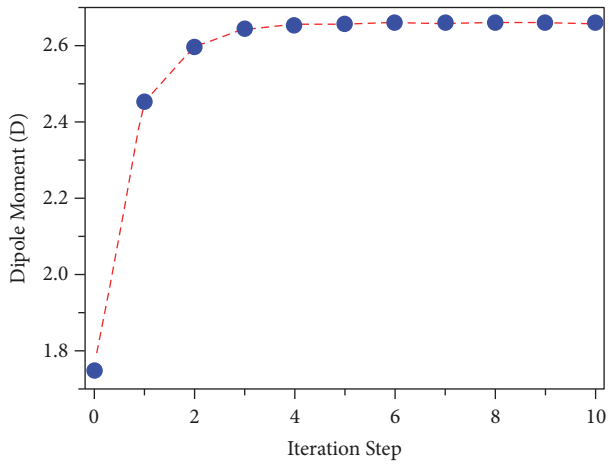


Figure 13: Evolution of values of the dipole moment of the EPAF crystal with the respective iteration numbers.

The EPAF crystal presents a rapid convergence in the dipole moment through the SM approach [25] (see Figure 13).

The quantum molecular calculations were performed with the Gaussian 09 program package [21]. For the calculation of $\chi^{(3)}(-\omega; \omega, \omega, -\omega)$, we used a small frequency [27, 28], estimate of the second frequency-dependent hyperpolarizability ($\langle\gamma(-\omega; \omega, \omega, -\omega)\rangle \cong 2\langle\gamma(-\omega; \omega, 0, 0)\rangle - \langle\gamma(0; 0, 0, 0)\rangle$) associated to a nonlinear optical process [29] of the intensity dependent refractive index (IDRI) from dc-K results. Table 5 shows the values of the EPAF when we consider the environment via the SM.

Table 6 presents the DFT prediction and the experimental results of the macroscopic quantities studied. The values of EPAF crystal are therefore 24.51, 2953, 3413, and 2866 times higher, respectively, than the values found experimentally by Prabhu et al. [17] (see Table 6).

The high value of the third-order electric susceptibility $\chi^{(3)}$ indicates the crystal as a promising candidate for NLO applications in photonic and optoelectronic devices.

## 4. Conclusions

In this work, using the DFT/B3LYP/6-311+G(d) calculation level, the effects of several solvent media on the geometric and the electric parameters of a Schiff base derivative (E)-4-[({4-[(piridin-2-ilmetilideno)amino]fenil}amino)-metil]fenol (EPAF) [15] were studied. A Hirshfeld surface analysis is presented to complement the EPAF crystal study of [15]. The fingerprints plots show that the interaction with greater percentage in the whole crystal is the H..H with 45.8% of the interactions followed by the C...H with 34.2% of the interactions. The geometry optimization was performed in the gas phase and in various solvent media. The overlap between the X-ray data for the EPAF and the DFT results in several solvent media showed a significant deviation of the RMSD parameter. Also in chloroform, the torsion angles $C4 - C7 - N1 - C8$ and $C11 - N2 - C14 - C15$ change from -166.3 (X-ray data) to +176.24 and of +176.4 (X-ray data) to -177.72°, respectively. This effect occurs for all solvents studied here and was due to the negative charge transfer to the hydroxyl bond to the terminal phenolic ring (C1–C6).

The NLO properties of the EPAF molecule in several solvent media were studied, and the static electric parameters values of the total dipole moment, linear polarizability, first hyperpolarizability, and the second hyperpolarizability increase with the increasing of the dielectric constant value of the solvent medium. The dispersion relation of the HRS first hyperpolarizability showed two resonant regions for $\omega >$ 0.06 a.u.. The gap energies were calculated from the HOMO-LUMO energy difference in several solvent media calculated and the values go from 3.466 eV ($\varepsilon$=1.0) to 3.349 eV ($\varepsilon$=182.4).

The p-nitroaniline (pNA) is used as a critical parameter for comparative studies because it has good NLO properties. The first-order dynamic hyperpolarizability of the molecule p-nitroaniline dissolved in chloroform is $\beta_{HRS}^{PNA} = 17.5 \times 10^{-30} cm^3/esu$ at 1064 nm [30, 31]; the EPAF in chloroform is $\beta_{HRS}^{EPAF} = 80.75 \times 10^{-30} cm^3/esu$, about 5 times greater than PNA.

The value of the third-order electric susceptibility $\chi^{(3)}$ of the EPAF crystal is ($6793.08 \times 10^{-22}\ m^2/V^2$) for the dynamic

case ($\lambda = 532\ nm$), thus 24.51 times higher than the values found experimentally by Prabhu et al. [17].

Thus, based on the magnitude of the dynamic HRS first hyperpolarizability in chloroform and the third-order electric susceptibility of the EPAF crystal, we can conclude that the EPAF offers potential applications to the development of materials with NLO properties.

## Data Availability

No data were used to support this study.

## Conflicts of Interest

The authors declare that they have no conflicts of interest.

## Acknowledgments

The authors would like to thank the following Brazilian agencies for financial support: Conselho Nacional de Desenvolvimento Científico e Tecnológico (CNPq), Coordenação de Aperfeiçoamento Pessoal de Nível Superior (CAPES); Pró-reitoria de Pesquisa e Pós-Graduação da PUC-GO (Prope) and Fundação de Apoio à Pesquisa do Estado de Goiás (FAPEG). Research was developed with support of the High Performance Computing Center at the Universidade Estadual de Goiás (UEG).

## Supplementary Materials

All Tables S1 - S23 are in the Supplementary Materials. *(Supplementary Materials)*

## References

[1] E. Timurdogan, C. V. Poulton, M. J. Byrd, and M. R. Watts, "Electric field-induced second-order nonlinear optical effects in silicon waveguides," *Nature Photonics*, vol. 11, no. 3, pp. 200–206, 2017.

[2] L. Lu, Z. Liang, L. Wu et al., "Few-layer bismuthene: sonochemical exfoliation, nonlinear optics and applications for ultrafast photonics with enhanced stability," *Laser & Photonics Reviews*, vol. 12, no. 1, Article ID 1700221, pp. 1–10, 2018.

[3] R. Salvi, C. Cerqueira-Coutinho, E. Ricci-Junior et al., " Diagnosing lung cancer using etoposide microparticles labeled with 99m Tc ," *Artificial Cells, Nanomedicine and Biotechnology*, vol. 46, no. 2, pp. 341–345, 2017.

[4] M. Luo, F. Liang, Y. Song et al., "$M_2B_{10}O_{14}F_6$ (M = Ca, Sr): two noncentrosymmetric alkaline earth fluorooxoborates as promising next-generation deep-ultraviolet nonlinear optical materials," *Journal of the American Chemical Society*, vol. 140, no. 11, pp. 3884–3887, 2018.

[5] H. Zhao, S. Han, and R. Hui, "Nonlinear optical spectroscopy of two-dimensional materials qiannan cui," 2017.

[6] M. Nakano, "Open-shell-character-based molecular design principles: applications to nonlinear optics and singlet fission," *The Chemical Record*, vol. 17, no. 1, pp. 27–62, 2017.

[7] G. Shi, Y. Wang, F. Zhang et al., "Finding the next deep-ultraviolet nonlinear optical material: $NH_4B_4O_6F$," *Journal of the American Chemical Society*, vol. 139, no. 31, pp. 10645–10648, 2017.

[8] R. Mallah, M. C. Sreenath, S. Chitrambalam, I. H. Joe, and N. Sekar, "Excitation energy transfer processes in BODIPY based donor-acceptor system - Synthesis, photophysics, NLO and DFT study," *Optical Materials*, vol. 84, pp. 795–806, 2018.

[9] A. N. Castro, L. R. Almeida, M. M. Anjos et al., "Theoretical study on the third-order nonlinear optical properties and structural characterization of 3-Acetyl-6-Bromocoumarin," *Chemical Physics Letters*, vol. 653, pp. 122–130, 2016.

[10] R. Medishetty, J. K. Zaręba, D. Mayer, M. Samoć, and R. A. Fischer, "Nonlinear optical properties, upconversion and lasing in metal–organic frameworks," *Chemical Society Reviews*, vol. 46, no. 16, pp. 4976–5004, 2017.

[11] Y. B. Rasal, R. N. Shaikh, M. D. Shirsat, S. Kalainathan, and S. S. Hussaini, "The investigation of potassium tetra thiourea chloride on linear-nonlinear optical, electrical and mechanical properties of KDP crystal for NLO applications," *Ferroelectrics*, vol. 520, no. 1, pp. 59–74, 2017.

[12] M. Anis, G. G. Muley, V. G. Pahurkar, M. I. Baig, and S. R. Dagdale, " Influence of Nd 3+ on zinc tris-thiourea sulphate single crystal: a comparative crystal growth, structural, linear–nonlinear optical and dielectric study to explore NLO device applications ," *Materials Research Innovations*, vol. 22, no. 2, pp. 99–106, 2016.

[13] P. K. Johansson, L. Schmüser, and D. G. Castner, "Nonlinear optical methods for characterization of molecular structure and surface chemistry," *Topics in Catalysis*, vol. 61, no. 9-11, pp. 1101–1124, 2018.

[14] R. Lozier, R. Bogomolni, and W. Stoeckenius, "Bacteriorhodopsin: a light-driven proton pump in Halobacterium Halobium," *Biophysical Journal*, vol. 15, no. 9, pp. 955–962, 1975.

[15] M. S. Faizi, N. Dege, and T. S. Iskenderov, "Crystal structure and DFT study of (*E*)-4-[({4-[(pyridin-2-ylmethylidene)amino]phenyl}amino)methyl]phenol," *Acta Crystallographica Section E: Crystallographic Communications*, vol. 74, no. 3, pp. 410–413, 2018.

[16] C. Reichardt, *Solvents and Related Titles from WILEY-VCH Organic Synthesis Workbook II Chemical Synthesis Using Supercritical Fluids*, 2003.

[17] S. R. Prabhu, A. Jayarama, K. Chandrasekharan, V. Upadhyaya, and S. W. Ng, "Synthesis, growth, structural characterization, Hirshfeld analysis and nonlinear optical studies of a methyl substituted chalcone," *Journal of Molecular Structure*, vol. 1136, pp. 244–252, 2017.

[18] J. J. McKinnon, D. Jayatilaka, and M. A. Spackman, "Towards quantitative analysis of intermolecular interactions with Hirshfeld surfaces," *Chemical Communications*, no. 37, p. 3814, 2007.

[19] R. Bersohn, Y. Pao, and H. L. Frisch, "Double-quantum light scattering by molecules," *The Journal of Chemical Physics*, vol. 45, no. 9, pp. 3184–3198, 1966.

[20] T. Verbiest, K. Clays, and V. Rodriguez, *Second-Order Nonlinear Optical Characterization Techniques An Introduction*, CRC Press, 2009.

[21] M. Frisch, G. W. Trucks, H. B. Schlegel et al., "Gaussian 09, revision D. 01," 2009.

[22] S. R. Wang, M. Arrowsmith, J. Böhnke et al., "Engineering a small HOMO-LUMO gap and intramolecular C–H borylation by diborene/anthracene orbital intercalation," *Angewandte Chemie International Edition*, vol. 56, no. 27, pp. 8009–8013, 2017.

[23] I. T. Lima, L. Sousa, L. Antonio, R. Junior, R. Tim, and S. Filho, "A DFT study of a set of natural dyes for organic electronics," *Journal of Molecular Modeling*, pp. 1–9, 2017.

[24] K. Srinivas, S. Sitha, V. J. Rao et al., "First hyperpolarizability of some nonconjugated donor–acceptor 3D molecules: non-centrosymmetric crystal through conformational flexibility," *Journal of Materials Chemistry*, vol. 15, no. 9, pp. 965–973, 2005.

[25] C. Valverde, F. A. Osório, T. L. Fonseca, and B. Baseia, "DFT study of third-order nonlinear susceptibility of a chalcone crystal," *Chemical Physics Letters*, vol. 706, pp. 170–174, 2018.

[26] K. Senthil, S. Kalainathan, A. R. Kumar, and P. G. Aravindan, "Investigation of synthesis, crystal structure and third-order NLO properties of a new stilbazolium derivative crystal: a promising material for nonlinear optical devices," *RSC Advances*, vol. 4, no. 99, pp. 56112–56127, 2014.

[27] S. Marques, M. A. Castro, S. A. Leão, and T. L. Fonseca, "Second hyperpolarizability of the calcium-doped lithium salt of pyridazine Li–H 3 C 4 N 2 ⋯ Ca," *Chemical Physics Letters*, vol. 659, pp. 76–79, 2016.

[28] D. M. Bishop and D. W. De Kee, "The frequency dependence of nonlinear optical processes," *The Journal of Chemical Physics*, vol. 104, no. 24, pp. 9876–9887, 1996.

[29] M. Maldonado, H. T. Baltar, A. S. Gomes et al., "Coupled-plasmon induced optical nonlinearities in anisotropic arrays of gold nanorod clusters supported in a polymeric film," *Journal of Applied Physics*, vol. 121, no. 14, Article ID 143103, 2017.

[30] P. Franzen, S. Zilio, A. Machado et al., "Experimental and theoretical investigation of first hyperpolarizability in aminophenols," *Journal of Molecular Structure*, vol. 892, no. 1-3, pp. 254–260, 2008.

[31] P. L. Franzen, L. Misoguti, and S. C. Zilio, "Hyper-Rayleigh scattering with picosecond pulse trains," *Applied Optics*, vol. 47, no. 10, Article ID 1443, 2008.

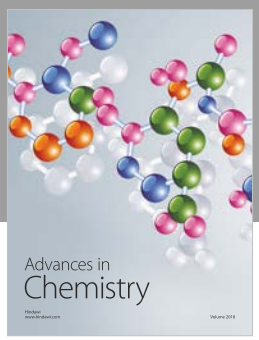

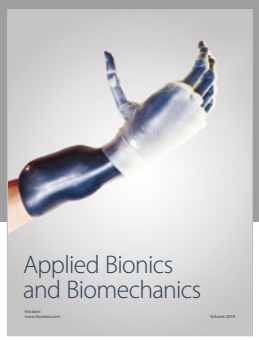

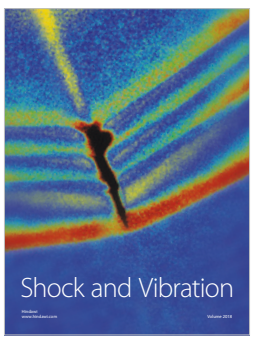

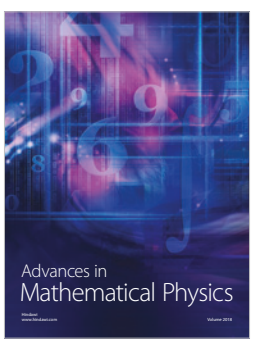

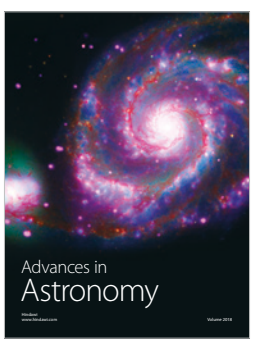

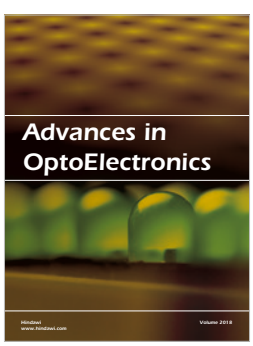

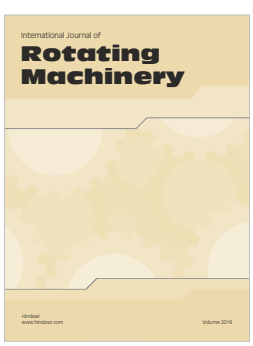

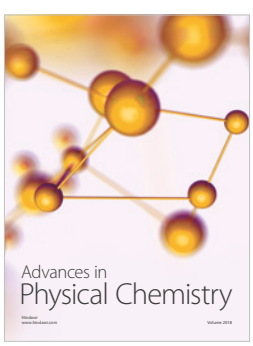

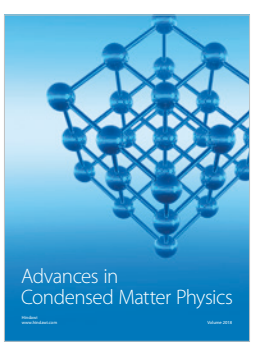

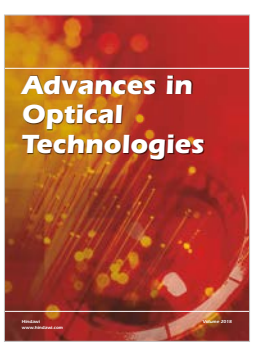

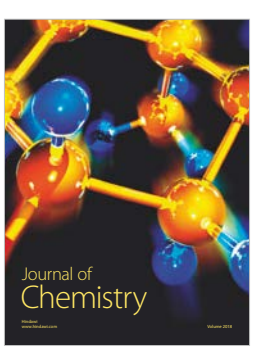

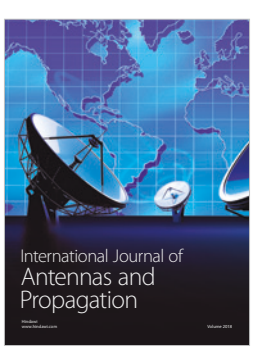

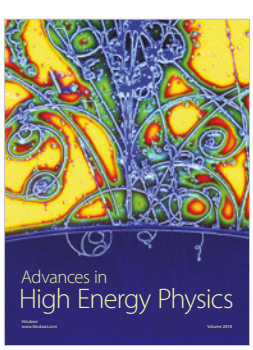

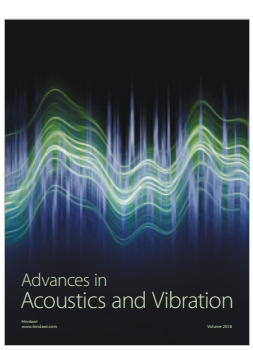


Hindawi

Submit your manuscripts at
www.hindawi.com